Anomalous transport dependence on Péclet number, porous medium heterogeneity, and a temporally varying velocity field

Alon Nissan* and Brian Berkowitz
Department of Earth and Planetary Sciences, Weizmann Institute of Science, Rehovot 7610001, Israel

(Received 12 July 2018; revised manuscript received 23 October 2018; published 7 March 2019)

We investigate the effects of the Péclet number (Pe) on transport of an inert chemical tracer in heterogeneous porous media. We simulate fluid flow and transport through two-dimensional pore-scale matrices with varying structural complexity. With increasing Pe, the anomalous nature of the transport becomes enhanced as the host domain becomes more heterogeneous, due to the increasingly dominant effects of the complex velocity field. The sensitivity of (anomalous) transport to Pe is shown to be controlled by the medium structure. We quantify the effects of Pe by interpreting the numerical simulations within the continuous time random walk method (CTRW) framework, and incorporating Pe within the underlying tracer transition time distribution. We then investigate transport behavior subjected to temporal variation in the velocity field magnitude, accounting for tracer propagation controlled by Pe. Because of the nonlinear influence of Pe on the transport behavior, we show that temporal variations in the velocity field can lead to an increase in the anomalous nature of the transport.

DOI: 10.1103/PhysRevE.99.033108

I. INTRODUCTION

A detailed understanding of chemical transport in natural porous media, such as geological formations, is essential for many technological and environmental processes [1]. However, due to the irregular structure of such media [2]—which leads to flow fields displaying complex spatiotemporal organization [3–5]—predicting transport dynamics within them is often elusive. The structural complexity of geological porous media often causes chemical transport to exhibit anomalous behavior [3], in the sense that the first and second (spatial and temporal) moments of the chemical plume are either space- or time-dependent and different from their Gaussian-based counterparts [6].

The origin of this anomalous behavior stems from the occurrence of non-Gaussian, multiscale velocity distributions (as opposed to a Gaussian distribution, as assumed within the classical advection-dispersion model). Propagation of a chemical species, whether inert or reactive, in such a domain often exhibits a temporal behavior that evolves toward an asymptotic state [7–9].

In this context, the formation of preferential paths and stagnant zones in natural porous media causes the tracer-weighted velocity distribution, Ω_p (which is the velocity field that is sampled by the transported chemical species, weighted by the actual proportion of tracers that interrogate each velocity) to deviate strongly from the fluid velocity distribution, Ω_f [5,10–12]. Therefore, for many situations—especially when the porous medium is characterized by strong spatial heterogeneity (as in natural geological formations)—prior knowledge about the fluid velocity field is insufficient to enable description of chemical tracer propagation within it. The convergence (or at least approach) of Ω_p to Ω_f depends on the ability of the tracer to sample, spatially, essentially the entire flow field; note that Ω_p converges precisely to Ω_f only if the domain is highly homogeneous with a uniform flow field. In highly heterogeneous domains, fluid flow is concentrated into a limited number of relatively narrow preferential pathways, so that a tracer can ultimately sample much of the domain only via molecular diffusion, over relatively long times [13–16]. Moreover, a recent study of the effect of inlet boundary conditions (uniform or flux-weighted) on the evolution of Lagrangian tracer velocities in heterogeneous fractured networks [17] showed that the different resulting initial tracer velocity distributions might have a persistent impact on transport behavior.

The ability of a tracer to sample the fluid velocity throughout the domain depends mainly on time; as shown experimentally [4], for example, Ω_p approaches Ω_f as the residence time increases. Thus, porous materials that are characterized by relatively homogeneous pore space configurations will tend to enable sampling of the full (spatial) velocity field spectrum much faster than in heterogeneous porous media [7]. A second factor, also related to time, is the interplay between the two main physical processes that control the transport behavior, advection, and molecular diffusion. In natural formations, the pattern of advective transport, which is derived directly from solution of the Navier-Stokes equations at the pore scale, and from the Darcy equation at larger (continuum) scales, often exhibits well-defined preferential channels and stagnant zones, which reduce the spatial sampling capacity of the tracer and lead to anomalous transport behavior. Conversely, the random movement of molecular diffusion enhances homogenization of the spatial sampling by tracers, by random jumps between fluid streamlines [18], and thus reduces the degree of anomalous transport.

The continuous time random walk (CTRW) framework is attractive for quantifying the evolution of chemical transport in natural porous media [6,19,20], CTRW treats tracer

*alon.nissan@weizmann.ac.il

motion by considering "particles" undergoing various types of transitions. These transitions encompass both the displacement due to structure and heterogeneity as well as the time taken to make the particle movement between, e.g., pores or fracture intersections [21]. The structural complexity of natural porous media leads to a wide spectrum of transition rates [4], which usually leads to a time-dependent transport regime that can ultimately converge to a Gaussian regime when the entire spectrum of transitions is sampled [8,20]. The time to reach such asymptotic behavior depends on the character of the space-time transition distributions [3], which are derived from analysis of the mechanisms controlling tracer propagation within the porous medium. Dentz *et al.* [8] studied the evolution of Lagrangian velocity in heterogeneous flows fields through a CTRW approach. They showed that the transport evolution (in terms of mean velocity and dispersion coefficient) toward asymptotic behavior is highly dependent on (stationary versus nonstationary) flow conditions, which suggests that the transition functions are modified accordingly.

The purpose of this study is to quantify the effect of the Péclet number, Pe, which encompasses the interplay between advection and molecular diffusion, on transport behavior of conservative (nonreactive) chemical species through porous media having various heterogeneous structural configurations. Within these domains, we solve for fluid flow (Navier-Stokes equations) and simulate chemical transport (streamline-based particle tracking, with molecular diffusion) at the pore scale. We then interpret the results within the CTRW framework and incorporate the effects of Pe within the underlying tracer transition time distribution. Subsequently, we use these distributions to examine the effects of a temporally fluctuating velocity field, so that Pe changes with time, on the spatiotemporal evolution of the propagating chemical plume.

II. METHODS

To understand the relation between Pe and porous medium heterogeneity, we generated three types of two-dimensional, porous media systems. Each system was assembled from a pore-scale image adapted from a natural rock material [22]. This image formed the basic template ("unit") for the porous media we consider; this unit was then modified twice by scaling (enlarging) the solid phase, uniformly around the perimeter of each solid grain, to obtain three topologically similar porous "units" with porosities of 0.32, 0.45, and 0.58 [12]. These units were then used to assemble the three configurations, where each system was constructed differently (Fig. 1): (1) statistically homogeneous system (SHS), constructed from a single unit type (with porosity of 0.45), (2) weak correlation system (WCS), composed using all three units, with no correlation between the units (i.e., the system was assembled randomly from the different units), and (3) strong correlation system (SCS), composed using all three units, where there is a spatial correlation among the different units (correlation length of four units, equal to 1 cm in space). Note that we use the terms "weak" and "strong" to indicate that the spatial correlation in the WCS exists within each unit (at the pore level), while in the SCS, the spatial correlation exists also among the units themselves. More information on the correlation maps can be found in Appendix A. While some individual units have a relatively high porosity (though not unrealistic, for cavities, channels, and lenses rich in organic material in natural rock formations), the average porosity of each system was 0.45. Each system was composed of (32×24) 768 units (each unit with dimensions 0.25 cm $\times$ 0.25 cm), with an average porosity of 0.45 and overall dimensions of 8 cm (width) $\times$ 6 cm (height). Below, we refer to the order SHS $\rightarrow$ WCS $\rightarrow$ SCS as an increase in heterogeneity.

Fluid flow through these systems was determined by solving the Navier-Stokes equations (using COMSOL Multiphysics) for steady, incompressible flow: $\rho(\mathbf{U}\cdot\boldsymbol{\nabla}\mathbf{U}) = -\boldsymbol{\nabla}p + \mu\nabla^{\mathbf{2}}\mathbf{U}$; $\boldsymbol{\nabla}\cdot\mathbf{U} = 0$, where $\mathbf{U}$ is the pore-scale (local) fluid velocity, p is the fluid pressure, and ρ is the fluid density. No-slip conditions were applied at the fluid-solid interface. A constant velocity was specified in the direction normal to the inlet boundary (Fig. 1, left side), and a constant reference pressure was prescribed at the outlet (Fig. 1, right side). The remaining (horizontal) boundaries were treated as impermeable. These conditions are representative of many experimental setups [23,24].

The Reynolds number, Re, in the simulations is defined as $\mathrm{Re} = \rho d_s \bar{U}_f/\mu$, where $\bar{U}_f$ is the average, pore-scale fluid velocity and d_s is the average diameter (1 mm) of the solid grains. The fluid velocity field was evaluated in a grid containing 6400 $\times$ 4800 (x, y axes) uniform cells, with spatial dimensions of $\Delta x = \Delta y = 1.25 \times 10^{-5}$ m for each cell. Conservative chemical transport was modeled by following an ensemble of particles that move according to the Langevin equation, $d\mathbf{x}(t) = \mathbf{v}[\mathbf{x}(t)]\,dt + \zeta\sqrt{2D_m\,dt}$, where $\mathbf{v}[\mathbf{x}]$ is the Lagrangian velocity vector. The advective displacement was modeled by a semianalytic streamline-based method [25] that employs the fluid velocity field, while the diffusive displacement was treated by a random walk method (where ζ is a $\mathcal{N}[0, 1]$ random number, and $D_m = 10^{-9}$ m^2/s is the coefficient of molecular diffusion). The time step dt was determined by the time needed for a particle to exit its current cell (on the numerical grid) and arrive to the adjacent cell (in the direction of flow). Therefore, dt is varying for each particle trajectory and among particles [25]. In addition, we restricted the maximum diffusive displacement allowed to at least one order magnitude smaller than the grid size [i.e., $dt \leqslant \frac{(0.1\Delta x)^2}{2D_m}$]. Particles ($5 \times 10^5$) were introduced along the inlet boundary by a flux-weighted pulse injection for $t \leqslant 0.1T_f$, where T_f is the final simulation time, which itself was proportional to the average fluid velocity ($\bar{U}_f$). The Pe is defined here as $\mathrm{Pe} \equiv \bar{U}_p\lambda^{-1}/D_m$, where $\bar{U}_p$ is the mean particle (transport) velocity over space and time, and λ^{-1} is the average displacement length of particle transitions (as discussed below in Sec. III A). Note that this definition distinguishes between fluid flow and tracer transport and employs a velocity ($\bar{U}_p$) that accounts for the mean tracer propagation; in heterogeneous domains, the average fluid and particle velocities can differ significantly, as noted in the Introduction (Sec. I). The range of Pe values considered here was $10^0 \leqslant \mathrm{Pe} \leqslant 10^3$ (and flow was within the laminar regime, $\mathrm{Re} < 10^{-3}$), which is common for transport in geological materials [1,2].

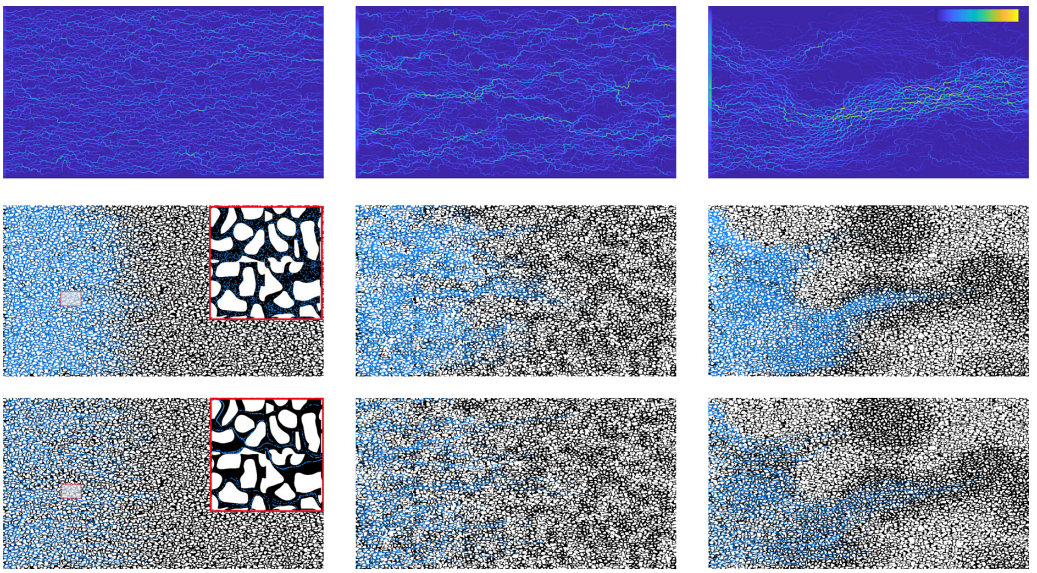

FIG. 1. Fluid velocities and tracer migration in the three porous media systems. Upper row: Normalized ($\mathbf{U}/\bar{U}_f$) velocity field for the different systems (from left to right): homogeneous system (SHS), randomly heterogeneous system (WCS), and structured heterogeneous system (SCS); the color bar represents relative velocity, with dark blue being lowest. Plume patterns of an inert tracer (blue dots) at Pe = 1 (middle row) and at Pe = 100 (lower row) for the different systems (white color indicates solid phase; black color indicates liquid phase). The tracer plumes are shown at the end of the injection time, prescribed as 10% of the final time of each simulation. The insets in the first plots of the middle and lower rows show the pore-scale distributions at tracer; note the more diffuse pattern at Pe = 1.

III. RESULTS

As a starting point, we show in Fig. 1 the effect of structural heterogeneity on the flow pattern (Fig 1, upper row), and on the transport propagation (Fig. 1, middle and lower rows). It can be seen that as the medium heterogeneity increases (left to right), the flow field becomes more preferentially oriented. In addition, the effect of different Pe values is also clearly visible (Fig. 1, middle and lower rows); at lower Pe, the tracers are spread more "uniformly" along the streamlines. This highlights the importance of Pe on the mixing and spreading of chemical species in porous media.

A. From numerical simulations to CTRW formulation

To analyze the effects of Pe on the transport behavior, considering also the different heterogeneous configurations, we use the CTRW framework [3,19]. The CTRW generalizes the random walk process from discrete time to continuous time with the spatial state description remaining discrete, $R(\mathbf{s},t) = \sum_{\mathbf{s}'} \int_0^t \psi(\mathbf{s}-\mathbf{s}', t-t') R(\mathbf{s}', t')\, dt'$, where $R(\mathbf{s},t)$ is the probability per time for a walker (tracer particle) to just arrive at site $\mathbf{s}$ at time t and $\psi(\mathbf{s},t)$ is the probability per time for a displacement $\mathbf{s}$ with a difference of arrival times of t. The probability density function (PDF) $\psi(\mathbf{s},t)$, the heart of the CTRW, determines the nature of the transport. Clearly, to evaluate $\psi(\mathbf{s},t)$ from the numerical simulations, the correlation between travel distance ($\mathbf{s}$) and travel time (t) for each (space-time) particle transition must be accounted for properly.

The first adaptation of the CTRW formulation [19] to geological formations was done by Berkowitz and Scher [6], who examined transport in random fracture networks. The consideration of fractured domains was convenient in the sense that the space-time transitions are discrete and straightforward to define; $\psi(\mathbf{s},t)$ was derived by recording the transitions ($\mathbf{s}$ and t) between the fracture intersections (i.e., between different fracture segments). To evaluate a solution of the CTRW equations, these authors invoked independence between the space and time transitions, based on analysis of the simulations, and employed a decoupled form, $\psi(\mathbf{s},t) = \psi(t)F(\mathbf{s})$, where $\psi(t)$ and $F(\mathbf{s})$ are the time and space transition distributions, respectively. The distribution $F(\mathbf{s})$ was assessed from the fracture network geometry—based on the segment length distribution between the fracture intersections— and $\psi(t)$ was derived by solving the velocity field within the domain and extracting the transition times. Particle tracking simulations through these networks were shown to exhibit the same dynamics as the CTRW theory.

Bijeljic *et al.* [7] simulated tracer transport in three-dimensional images of various natural rock samples and derived the temporal transition rate, $\psi(t)$, by considering a fixed transition length ($\mathbf{s}$ = voxel size of the numerical grid). The use of a fixed spatial transition means that the spatial correlations in the tracer transitions are considered (or assumed to be) negligible [i.e., $F(\mathbf{s})$ is constant]; this assumption can be reasonable for relatively homogeneous materials, but it is not necessarily appropriate when the flow field has strong spatial correlations in heterogeneous domains. Analysis of the velocity distribution in a fixed spatial grid demonstrates obvious, strong correlations from cell to cell along streamlines (preferential pathways). Such cell-to-cell correlations were shown in numerical simulations [26], but this information—known correlations affecting particle transitions—was then neglected in a particle-tracking algorithm based on CTRW, but incorrectly called "classical CTRW." As formulated originally by Scher and Lax [27] and Scher and Montroll [28], and adapted subsequently for transport in porous and fractured

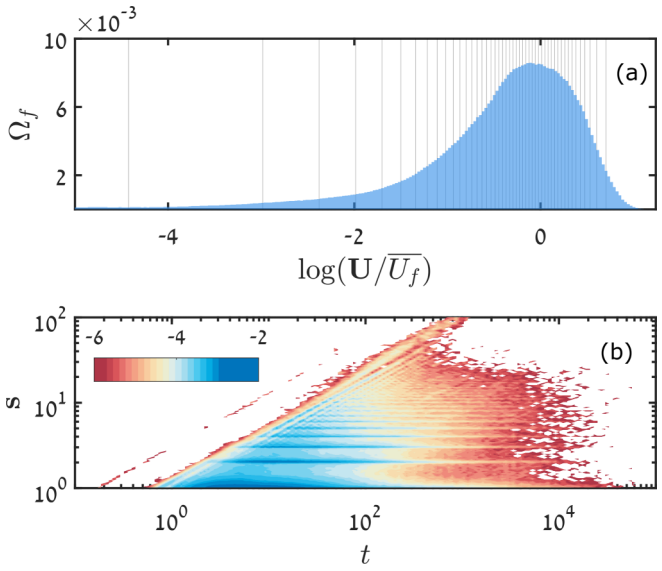

FIG. 2. (a) An example of the normalized probability density function (Ω_f) of the normalized fluid velocities ($\mathbf{U}/\bar{U}_f$), divided into 50 equally weighted velocity classes (areas divided by black lines). (b) An example of $\psi(\mathbf{s},t)$ derived from the numerical simulations. Note that these examples were derived from the WCS domain (see Appendix B for SHS and SCS systems) and that increasing the number of velocity classes does not change the general pattern of the results.

media by Berkowitz and Scher [6] and in many papers thereafter, "classical CTRW" (whether determined in terms of particle-tracking or partial differential equation solutions) incorporates these correlations naturally in a properly defined space-time probability density function describing the particle transitions. This point is demonstrated clearly by Berkowitz and Scher [29], who reanalyzed and discussed in depth the numerical simulations of Le Borgne *et al.* [26].

It has been shown [30] that if the PDF of displacements is compact, then the decoupled form of $\psi(\mathbf{s},t)$, i.e., $\psi(t)F(\mathbf{s})$ is often sufficient as a good representation of $\psi(\mathbf{s},t)$. Only if $F(\mathbf{s})$ has a power-law dependence on $\mathbf{s}$ (i.e., is Lévy-like), does the transport display sensitivity to the high-velocity part of the spectrum, so that a fully coupled $\psi(\mathbf{s},t)$ is needed. The choice of $F(\mathbf{s})$ is much more subtle in a porous medium with a network of pores, where there is no obvious structural arrangement as in a random fracture network [31].

To evaluate the CTRW functions in natural porous media, we divide Ω_f into equally weighted velocity classes, N [see Fig. 2(a) as an example for the WCS domain]. When a particle makes a transition between different velocity classes, the time (t) and distance ($\mathbf{s}$) required to complete this transition are recorded. Doing this for all particles gives the essential information needed to evaluate $\psi(\mathbf{s},t)$ of each system [see Fig. 2(b) as an example for the WCS; the SHS and SCS results show similar behavior and can be found in Sec. B 1 of the appendices). From the results (see Sec. B 1 in the appendices), we note that the number of velocity classes does not affect the general pattern of $\psi(\mathbf{s},t)$; hence the method of characterization employed here is seen to be relatively robust. Note that in Fig. 2, the time and length transitions are normalized by the grid length space (Δx) and the particle mean velocity (U_p); hence $\mathbf{s} = \mathbf{s}/\Delta x$ and $t = t/(\Delta x/U_p)$.

From the numerical simulations, $\psi(\mathbf{s},t)$ is characterized by a pattern of multiple peaks. This is an artifact of the particle-tracking algorithm (which records jumps from cell to cell) together with the concept of velocity classes (wherein a transition can be recorded only when a particle moves between cells). There is thus a preference for a particle to change velocity classes on the numerical grid itself; and hence there is higher probability to make a transition on the grid. Plotting Fig. 2 in normalized form shows that the higher probability for transitions occurs at integer values (i.e., Δx, $2\Delta x$, $3\Delta x$).

As noted above, $\psi(\mathbf{s},t)$ can be well approximated by a decoupled form $\psi(\mathbf{s},t) = \psi(t)F(\mathbf{s})$ as long as the spatial increment, $F(\mathbf{s})$, has a compact distribution. As can be seen in Fig. 2(b), analysis of the numerical simulations here, using this velocity-weighted class method of characterization, confirms that the spatial increment (y axis) has a relatively narrow distribution compared to the temporal increment distribution (x axis), which spans several orders of magnitude. Henceforth, we make a use of the uncoupled form $\psi(\mathbf{s},t) = \psi(t)F(\mathbf{s})$.

Figures 3(a) and 3(b) show the PDFs for the temporal and spatial transitions, respectively [i.e., $\psi(\tau)$ and $F(\ell)$], in the WCS system for different Pe, where $\tau \equiv t\bar{U}_p/\Delta x$, and $\ell \equiv \mathbf{s}/\Delta x$ are characteristic time and length, respectively (note that the results for the SHS and SCS systems exhibit similar behavior; see Sec. B 2 in the appendices). It is seen that the spatial increment, $F(\ell)$, is not affected by Pe [Fig. 3(b)], so that the spatial particle transition depends directly on the configuration of the velocity field (obtained by solving the Navier-Stokes equations) in each specific porous medium domain. Because the flow is laminar ($\mathrm{Re} \leqslant 10^{-3}$), the changes in the velocity field are linear (inertial forces are negligible: $\mathbf{U}\cdot\nabla\mathbf{U} \to 0$) [12], so that the partition of velocity classes is constant with respect to Pe. We find that $F(\ell)$ can be well approximated by an exponential distribution, $F(\ell) = \lambda\exp(-\lambda\ell)$, with mean transition length λ^{-1}; note that the value of λ^{-1}, in this case, is normalized by the characteristic length scale Δx. Analysis of the simulations shows that $({\lambda_{\mathrm{SHS}}}^{-1} = 2.56, {\lambda_{\mathrm{WCS}}}^{-1} = 3.12, {\lambda_{\mathrm{SCS}}}^{-1} = 3.61)$, as expected from the increasing spatial correlations of the different configurations. Because λ^{-1} represents the mean transition length between different velocity classes, we expect that the number of velocity classes (N) will affect its value. As the number of velocity classes used to characterize transport increases (i.e., as Ω_f is divided into more regions), the probability of a particle to jump between different classes increases, simply due to the finer resolution of the number of classes. In Fig. 4(a) we show the sensitivity of λ^{-1} (in normalized form) to N for the different porous systems. We plot the mean value of λ^{-1} over different Pe, together with the standard deviations with respect to Pe. It is seen that the number of velocity classes increases as λ^{-1} decreases. In addition, as the number of velocity classes increases, λ^{-1} approaches 1, indicating that the mean transition length is equal to the grid resolution. Hence, due to its asymptotic behavior, the relation between λ^{-1} and N shows a power-law dependence [Fig. 4(a), dashed line]. Note that as N increases (i.e., λ^{-1} decreases), $\psi(\mathbf{s},t)$ narrows, so that the probabilities of extreme transitions

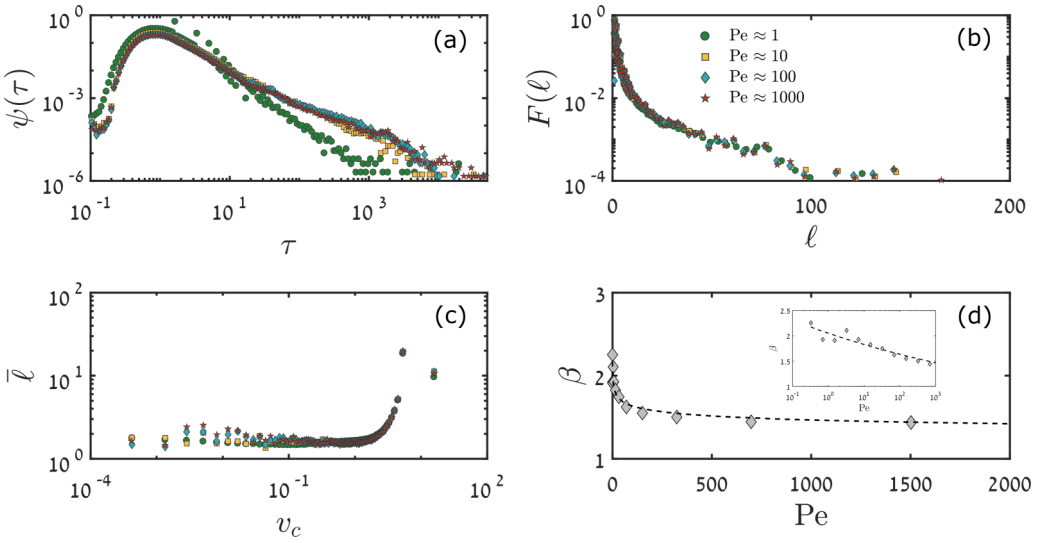

FIG. 3. (a) The probability $\psi(\tau)$ of a transition between two velocity classes, with different Pe. (b) The probability $F(\ell)$ of a displacement distance between two velocity classes, with different Pe. (c) The mean spatial displacement ($\bar{\ell}$) of each velocity class (v_c). (d) $\psi(\tau)$ power-law exponent, β, as a function of Pe. In the inset we show the results in semilog scale (x axis); the numerical simulations results are by the diamond symbols, and the dashed-black line indicates the power-law fit. Note that the results are shown for the WCS.

become smaller. However, this narrowing does not affect the general pattern of $\psi(\mathbf{s}, t)$ (see Fig. 8 in the appendices).

On the other hand, $\psi(\tau)$ shows significant dependency on Pe [Fig. 3(a)]. We find that $\psi(\tau)$ has a unique pattern (for all values of Pe) starting with an exponential increase accompanied by a power-law decline. We approximate this with a curved power-law function [32] (i.e., an inverse gamma distribution), $\psi(\tau) = C\exp(-t_1/\tau)\tau^{-1-\beta}$, where t_1 controls the exponential increase, β accounts for the power-law region, and $C \equiv \frac{{t_1}^{\beta}}{\Gamma(\beta)}$ is the PDF normalization factor with Γ the Gamma function. The peak of $\psi(\tau)$ can be evaluated from the derivative of the function: $\psi(\tau^*)_{\mathbf{t}} \equiv 0$, which leads to $\tau^* = \frac{t_1}{1+\beta}$, so that $t_1 = (1+\beta)\tau^*$. Inserting the expression for t_1 into $\psi(\tau)$ yields

$$\psi(\tau) = \frac{\exp\left[-\frac{(1+\beta)\tau^*}{\tau}\right]\left[\frac{(1+\beta)\tau^*}{\tau}\right]^{\beta}}{\tau\Gamma(\beta)}. \tag{1}$$

Figure 3(c) shows the mean spatial displacement ($\bar{\ell}$) of each velocity class (v_c). The results demonstrate the ability of tracer particles in the higher classes (higher velocities) to remain in their class (velocity), as compared to tracer particles in the slow-velocity regions. For the low-velocity classes, the mean spatial particle displacement ($\bar{\ell}$) increases with Pe because the role of molecular diffusion is weaker.

Within the CTRW framework (see Appendix C for more information), the mean particle velocity, v_ψ, and the generalized particle dispersion, D_ψ, are the first and the second spatial moments of $F(\mathbf{s})/\bar{t}$, where $\bar{t}$ denotes the mean time transition, defined as

$$v_\psi = \frac{\int_0^\infty F(\mathbf{s})s\,ds}{\int_0^\infty \psi(t)t\,dt} \quad \text{and} \quad D_\psi = \frac{1}{2}\frac{\int_0^\infty F(\mathbf{s})s^2\,ds}{\int_0^\infty \psi(t)t\,dt}. \tag{2}$$

We stress here that v_ψ in the CTRW is identical to the mean particle velocity $\bar{U}_p$ employed in the numerical analysis up to this point. For $1 < \beta < 2$, which is the common case when modeling transport in natural geological formations [24], we can derive an analytical solution for Eq. (2) with the expressions for $F(\mathbf{s})$ (exponential distribution) and $\psi(t)$ (curved power-law distribution). For one-dimensional problems, we obtain

$$v_\psi = \frac{\beta-1}{(\beta+1)\lambda\tau^*} \quad \text{and} \quad D_\psi = \frac{\beta-1}{(\beta+1)\lambda^2\tau^*}. \tag{3}$$

Thus the mean asymptotic particle velocity (v_ψ) is proportional to the generalized particle dispersion (D_ψ) multiplied by the medium length scale (λ). Because Pe is defined here as $\mathrm{Pe} = \frac{v_\psi \lambda^{-1}}{D_m}$ (note again that v_ψ replaces $\bar{U}_p$), there is a linear relation between D_ψ and Pe, for the range of Pe that was considered here ($10^0 \leqslant \mathrm{Pe} \leqslant 10^3$). Significantly, this linear behavior is consistent with many experimental and numerical studies that delineate the relationship between dispersion and Pe [31,33–35].

We now focus on the key relationship between Pe and the exponent β [Eq. (1)]. Because β denotes the slope of the power law that characterizes the nature of the (anomalous) transport, we argue that the two parameters must be linked to each other. We show that $\psi(\tau)$ is modified according to Pe, so that higher Pe values lead to a decrease in the power slope (i.e., β decreases), which in the context of transport indicates an increase in the anomalous behavior. The relation between β and Pe is shown in Fig. 3(d); for all systems a power-law dependence is exhibited, $\beta \propto \mathrm{Pe}^{-\xi}$ (with $\xi_{\mathrm{SHS}} = 0.064$, $\xi_{\mathrm{WCS}} = 0.081$, $\xi_{\mathrm{SCS}} = 0.084$ for the three systems examined here). As expected, higher spatial heterogeneity leads to larger ξ, which means that the sensitivity to Pe increases with heterogeneity. The fact that lower Pe shows less anomalous behavior is because displacements by molecular diffusion can reduce the residence time of the chemical tracers in stagnant zones within the flow field. In Fig. 4(b), we examine the effects of N on the general behavior of $\psi(t)$,

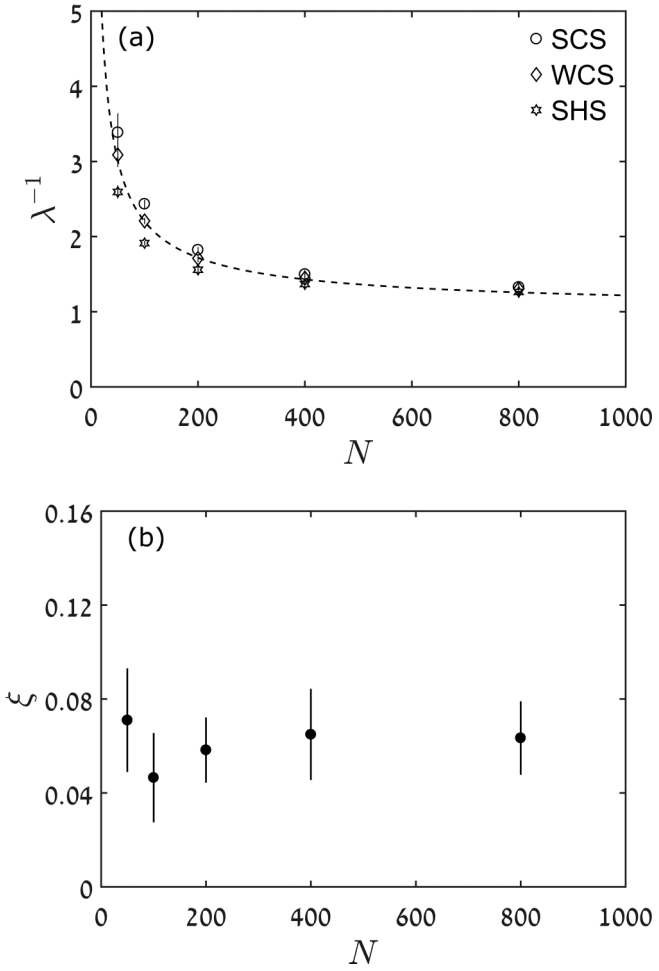

FIG. 4. (a) Mean transition length (λ^{-1}) as a function of the number of velocity classes (N), for the three porous systems: SHS (hexagrams), WCS (diamonds), and SCS (circles). This relation is well approximated by a power-law function (dashed line). Vertical black lines (on the symbols) represent the standard deviation among different Pe. (b) The average value of ξ (black circles) of the three porous systems (SHS, WCS, and SCS), for different numbers of velocity classes (N). Standard deviation among the systems is represented by vertical black lines.

with respect to Pe, through the value ξ. We plot the mean value of ξ (black circle) over the different porous materials; the standard deviation for each velocity class, between the different systems, is shown by a black vertical line. It is seen that the value of ξ does not change monotonically with respect to N, and that its value lies within the standard division for all cases. We conclude from these analyses that the shape of $\psi(t)$ is not sensitive to the number of velocity classes.

Because $\beta \propto \mathrm{Pe}^{-\xi}$ and $\tau^* = \frac{(\beta-1)\lambda^{-1}}{(\beta+1)v_\psi}$ [from Eq. (3)], we can quantify tracer transport behavior for different Pe via three parameters: v_ψ, λ, and ξ. For most problems, the first two parameters can be constrained (e.g., v_ψ by the Darcy velocity and λ by the pore throat and grain diameters), while ξ can by considered as a fitting parameter.

We point out here that while a truncated power law is often chosen as the form of $\psi(t)$ at continuum scales [3,20,24,36], as well as at the pore scale [7,31], a curved power law was chosen to match the numerical results presented here. From a physical point of view, the curved power law specifically quantifies the peak of $\psi(t)$ [recall Fig. 3(a)] and full character of the transition time distribution. Application of the truncated power law to continuum-scale problems, which does not display such a peak, can be justified because the short-time transitions often have little effect, in relative terms, on the overall transport dynamics [3]. In the context of truncated power-law analyses, too, it is noted that β can be constant over at least an order of magnitude variation in the macroscopic flow rate, at the continuum scale [24]. At the pore scale, it has been shown [7,31] that the truncated power law is very sensitive to Pe.

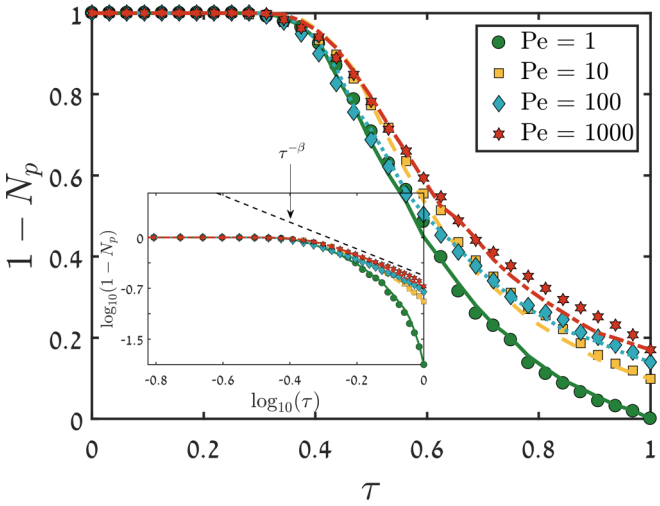

FIG. 5. Comparison between the numerical simulations (symbols) and the proposed CTRW model (lines).

Figure 5 shows a validation of the current CTRW formulation against the numerical simulations. For each value of Pe, and for each porous medium system, we record the particle breakthrough curve at the system outlet. We then use the CTRW parameters (i.e., β, t_1, and λ^{-1}) that were fit by a curved power-law function to the numerical simulation outputs [Figs. 3(a) and 3(b)]. Figure 5 compares the particle breakthrough curves (plotted as $1 - N_p$ to emphasize their tails) of the numerical simulations against the CTRW model [Eq. (3)], for different Pe (note that the results presented here are for the WCS; similar behavior was found for all systems). The results highlight the effect of Pe on the degree of anomalous transport, where higher values of Pe lead to longer residence times (longer tails), and thus increase the degree of anomalous transport behavior. The inset in Fig. 5 shows the results on a log-log scale, to highlight the power-law scaling $\tau^{-\beta}$ that is expected from the $\psi(\tau)$ distribution, Eq. (1); the dashed line shown in the inset shows $\tau^{-\beta}$, for $\beta = 1.5$ as seen in Fig. 3(d).

B. Effects of a fluctuating velocity field on transport dynamics

The nonlinear scaling of β with Pe may lead to unusual transport behavior when the flow fluid fluctuates over time (i.e., under a time-dependent velocity field) [37]. Rather than

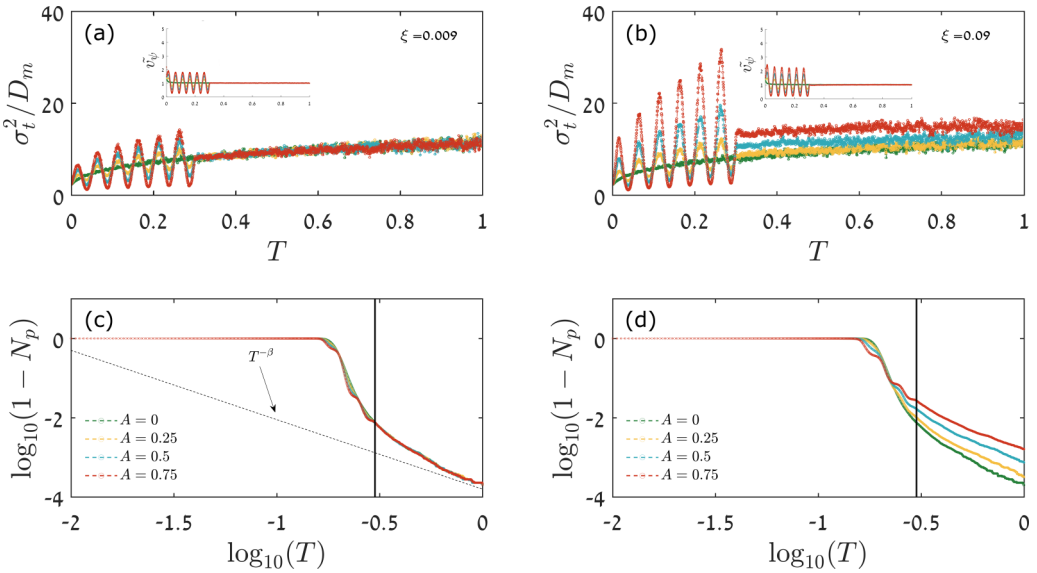

FIG. 6. Time-dependent, Monte Carlo simulations with 10^5 particles that propagate according to the CTRW method, for two systems that differ in terms of their sensitivity (ξ) to Pe. In each system, the effects of fluctuations (A) in velocity magnitude on (inert tracer) transport behavior are examined. Particle dispersion over time for (a) $\xi = 0.009$ and (b) $\xi = 0.09$, respectively; insets show the particle velocity over time. Reverse particle cumulative breakthrough curves over time for (c) $\xi = 0.009$ and (d) $\xi = 0.09$, respectively; vertical black lines indicate the end of the time-dependent period. The dashed line in panel (c) shows the power law $T^{-\beta}$ with $\beta = 1.75$, which characterizes the long-time slope of the BTCs.

velocity and tracer concentration fluctuations being averaged out, so that the system converges (over time) to mean behavior (i.e., characterized in terms of a mean velocity and dispersion), the nonlinear behavior might result in perturbation of the system to a different dynamical state.

To examine the effect of a time-dependent velocity field, we simulate tracer transport via a CTRW Monte Carlo particle-tracking algorithm, with a temporally varying inlet boundary condition for fluid velocity [37]. The algorithm samples particle transitions using an implementation of the temporal] $\psi(t)$, curved power-law distribution] and spatial ($F(\mathbf{s})$, exponential distribution) PDFs to determine the transport patterns of particles; in each case, 10^5 particles are injected as a pulse, at $t = 0$, along the left boundary of the domain. We explore particle propagation in two systems that differ in terms of their sensitivity to Pe. Recalling that $0.064 \leqslant \xi \leqslant 0.084$ in Sec. III A, we choose here systems with $\xi = 0.09$ and $\xi = 0.009$, the latter being a benchmark representing a highly homogeneous porous medium.

In each simulation, the mean particle velocity (v_ψ) is time-dependent [i.e., $v_\psi(t)$], and changes every time step (Δt) according to $v_\psi = \bar{v}_\psi[1 + A\sin(\frac{2\pi t}{B\bar{v}_\psi})]$ where $\bar{v}_\psi = 10^{-3}$ m/s is the mean transport velocity over the simulation time (constant for all cases), A is the amplitude, and $B = dt \times \bar{v}_\psi$ is the wavelength in the time dimension (constant for all cases). The time-dependent regime was limited to the first 30% of the simulations, after which a constant v_ψ was prescribed, and four different amplitudes ($A = 0, 0.25, 0.5, 0.75$) were considered. The value of Pe ($\text{Pe} \equiv v_\psi \lambda^{-1}/D_m$; with $\lambda^{-1} = 10^{-5}$ m and $D_m = 10^{-9}$ m^2/s constant for all cases) changes proportionally with changes in v_ψ; thus, β also varies nonlinearly. We write $\beta = \beta_0 \times \text{Pe}^{-\xi}$ and choose $\beta_0 = 1.75$ as a representative value for transport in natural porous materials [3]. Throughout the simulations, the variation in β—as a result of variation in v_ψ—did not exceed 18%.

The insets in Figs. 6(a) and 6(b) show the normalized center of mass velocity, $\tilde{v}_\psi \equiv v_\psi/\bar{v}_\psi$ for the cases $\xi = 0.009$ and $\xi = 0.09$. The particle velocities fluctuate around the mean up to $T = 0.3$ (where T is the simulation time normalized by its final value), at which point the fluctuation regime is halted and v_ψ is set to its mean value; this enables convenient comparison between the different magnitudes.

In Figs. 6(a) and 6(b) we examine the dispersive behavior resulting from the velocity fluctuations in the two systems, defining dispersion in terms of the temporal derivative of the particle variance, σ_t^2, normalized by the molecular diffusion ($D_m = 10^{-9}$ m^2/s). For the less sensitive ($\xi = 0.009$) domain, the particle variance converges to the same value—for all amplitudes—and the temporal fluctuation effects cannot be observed after the system stabilizes ($T > 0.3$). On the other hand, when the medium is more sensitive to Pe ($\xi = 0.09$), the particle variance does not converge after the velocity fluctuations end ($T = 0.3$), and we observe a gradual increase with the fluctuation magnitude (A). This latter case leads to different transport behaviors, where the degree of anomalous transport increases with the fluctuation amplitude [as can be seen by the breakthrough curve tails in Fig. 6(d)]. Figures 6(c) and 6(d) display the cumulative particle breakthrough curves (plotted as $1 - N_p$ to emphasize their tails), normalized by the total number of particles [$N_p(T)$]. For the $\xi = 0.009$ domain, the breakthrough curves are identical for all cases ($T > 0.3$), while for the $\xi = 0.09$ domain, the breakthrough curves show more anomalous behavior—in terms of early-time arrivals and late-time tails—as the fluctuation amplitude

increases. Note that the oscillations in the curves [Figs. 6(c) and 6(d)] are due to the undulating behavior of v_ψ (for $T < 0.3$), and they show a systematic increase and decrease as A increases and decreases. Note that after the period of temporal fluctuation ends ($T > 0.3$), all simulations (i.e., with different A) have the same transport parameters; and yet, there is a significant difference in breakthrough curves [Fig. 6(d)] among the different velocity amplitudes. This difference lies within the CTRW framework, which accounts for particle memory due to temporal correlations [3], which change with Pe [Figs. 3(a) and 3(d)]. Thus, each fluctuation amplitude (A) exhibits a different dispersion regime due to the role of memory.

IV. SUMMARY

We first illustrate (Fig. 1) that variation in Pe can lead to a modification in the transport behavior, and that the tracer spreading tends to become more homogeneous along fluid streamlines as Pe decreases. We quantify this effect via the CTRW framework, incorporating Pe into the underlying tracer transition time distribution (through β).

To evaluate the CTRW PDFs from the numerical simulations, we divide each fluid velocity distribution into different velocity classes, weighted uniformly along the velocity spectrum [Fig. 2(a)]. This provides the essential information to obtain the key CTRW PDF, $\psi(\mathbf{s}, t)$ [Fig. 2(b)], quantifying the evolution of a propagating tracer plume. Because $\psi(\mathbf{s}, t)$ is often characterized by a relatively compact distribution of spatial increments, compared to the temporal increments, we employ the decoupled form $\psi(\mathbf{s}, t) = \psi(t)F(\mathbf{s})$. From analysis of the numerical simulations, we obtain the shape of $F(\mathbf{s})$ [exponential distribution, Fig. 3(b)] and $\psi(t)$ [curved power-law distribution, Fig. 3(a)]. In this context, we show that the shape of the $F(\mathbf{s})$ is constant with respect to Pe and depends on the solution of the velocity field (i.e., the flow problem rather than the transport one). In addition we confirm through the numerical analysis—for the first time—that $F(\mathbf{s})$ has a compact distribution in representative natural porous media.

In contrast to the displacement transitions, the temporal transition function $\psi(t)$ is found to be sensitive to Pe, with higher Pe causing a decrease in the power-law exponent (β) of $\psi(t)$. This leads to an increase in the anomalous behavior of tracer transport. We find that the relation between β and Pe can be well approximated by a power dependence, with $\beta \propto \mathrm{Pe}^{-\xi}$. The sensitivity of the porous medium to Pe is characterized by the value of ξ, which increase with medium heterogeneity. Therefore, in natural environments, where spatial heterogeneity is significant, we expect that transport dynamics will be sensitive to Pe.

Furthermore, we examine the effects of different Pe on anomalous transport in scenarios that involve time-dependent velocity field conditions. We show (Fig. 6) that as a function of Pe and ξ, a time-dependent velocity field causes increased anomalous transport behavior, with increasing magnitudes of fluctuation amplifying these effects.

The findings here are significant in terms of understanding fundamental transport behavior of inert chemicals in geological porous media, under natural conditions, where the porous media are often characterized by strong spatial complexity and time-dependent flow fields.

ACKNOWLEDGMENT

The authors gratefully acknowledge support by the Israel Science Foundation (Grant No. 485/16).

APPENDIX A: GENERATING CORRELATION MAPS—AT THE PORE SCALE

To generate the system configurations (Sec. II) we used a basic code to produce two-dimension Gaussian fields (MATLAB files exchange). The generated fields consist of 768 cells (32×24), and their spatial dimensions are 8×6 cm (x, y). Figure 7(a) shows an arbitrary example of this kind of field; note that the color gradient is blue to yellow, and represents different scalar values. To produce the correlated fields [Fig. 7(a)], two variables are needed: the variance of the Gaussian distribution (σ) and a correlation length (ℓ). In this specific example, $\sigma = 1$ and $\ell = 1$.

To examine flow and transport in uniform distributed fields, as shown in the main text, the Gaussian fields generated here were converted to uniform fields. This was done by dividing each Gaussian distribution into equally weighted regions [Fig. 7(b)]. Note that because the Gaussian distribution is symmetric there is no meaning to the of the Gaussian distribution following division into weighted regions. Each region was then relabeled with a single value (e.g., 1, 2, 3,. . .), resulting in the Gaussian two-dimensional correlated map [Fig. 7(a)] being modified to a uniform correlated map [Fig. 7(c)] that consists of a limited number of units (regions). Note that there is an equal number of cells in each region.

In this study, three different units were used, which differ in terms of their porosity; the Gaussian distribution was thus divided into three regions [Fig. 7(d)] In addition, to increase the degree of heterogeneity, each pore-scale image (unit) was rotated randomly (i.e., 0°, 90°, 180°, or 270°).

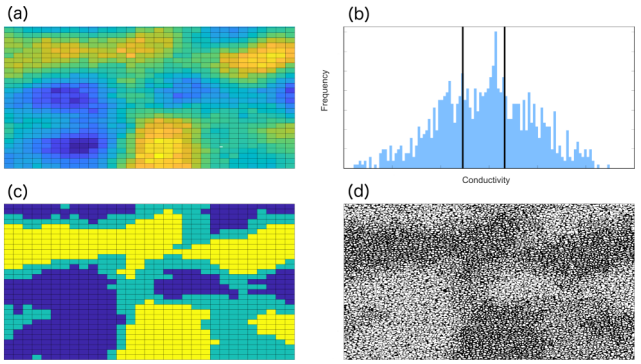

FIG. 7. (a) A two-dimensional, correlated field with a Gaussian distribution. (b) The Gaussian distribution of the correlated field, divided into three equally weighted regions (vertical black lines). (c) Modification of panel (a), where each region was labeled with a single value, and thus the two-dimensional field becomes a uniform correlated field. (d) Transformation from a field shown in panel (c) into a porous domain consisting of three different basic units.

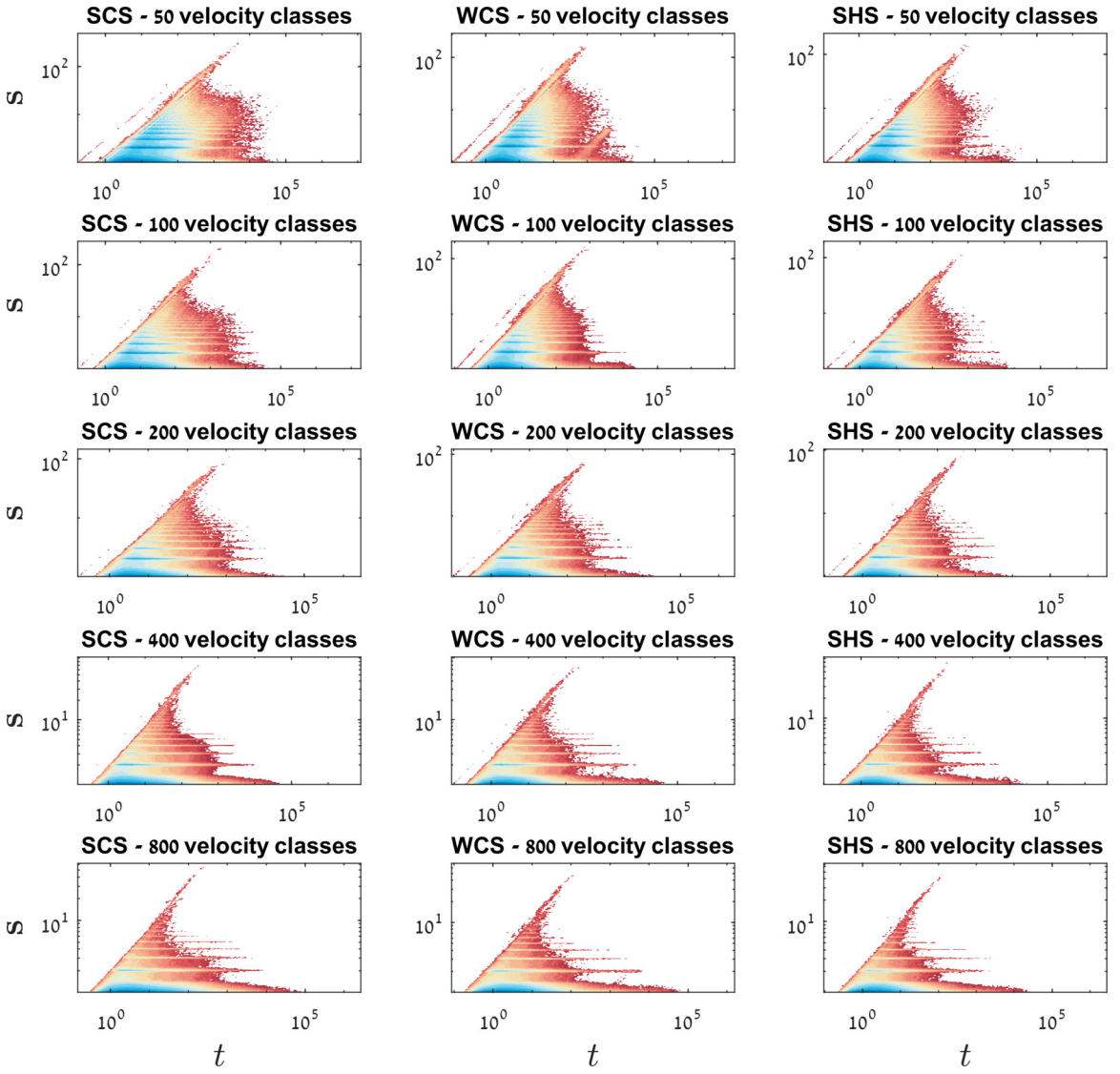

FIG. 8. Comparison between the effects of the number of velocity classes N on the shape of $\psi(\mathbf{s}, t)$. Sensitivities are shown for $N = 50$ (first row), 100 (second row), and 200 (third row), 400 (fourth row), and 800 (fifth row), for the three types of porous systems (i.e., SCS, WCS, and SHS).

APPENDIX B: VELOCITY CLASSES

In this section, the sensitivity of the number of velocity classes (N) to the shape of $\psi(\mathbf{s}, t)$ is examined.

1. Coupled $\psi(\mathbf{s}, t)$ case

In Sec. III A the coupled of $\psi(\mathbf{s}, t)$ is evaluated from the numerical results, using the concept of velocity classes. Figure 8 shows the sensitivity of the number of velocity classes (N) to the shape of $\psi(\mathbf{s}, t)$, using $N = 50$, 100, 200, 400, and 800 velocity classes, for the three porous systems (SCS, WCS, and SHS).

Clearly, the shape $\psi(\mathbf{s}, t)$ is not affected significantly by the number of velocity classes and demonstrates the robustness of this method of characterization. However, it is seen that the outer edges of $\psi(t)$ converge inwards velocity classes increases (from top to bottom in the figure). This is due to the fact that the probability to complete transitions for longer distances decreases as N increases (Figs. 3 and 4).

2. Decoupled $\psi(\mathbf{s}, t) = \psi(t)F(\mathbf{s})$ case

As discussed in the main text, $\psi(\mathbf{s}, t)$ can be simplified, in many cases, to a decoupled form $\psi(\mathbf{s}, t) = \psi(t)F(\mathbf{s})$, so that the space and time transitions are independent. Figure 9 shows that the decoupled form, as for the coupled case, is not particularly sensitive to the number of velocity classes.

It is clear from the results that the PDF of the displacement transitions is sensitive to the number of velocity classes; the PDF shows a smaller range as the number of velocity classes increases. This behavior was discussed in detail in the main text [Sec. III A and Fig. 4(a)]. In contrast, $\psi(t)$ does not show any significant change with N, which is supported by the results in Fig. 4(b).

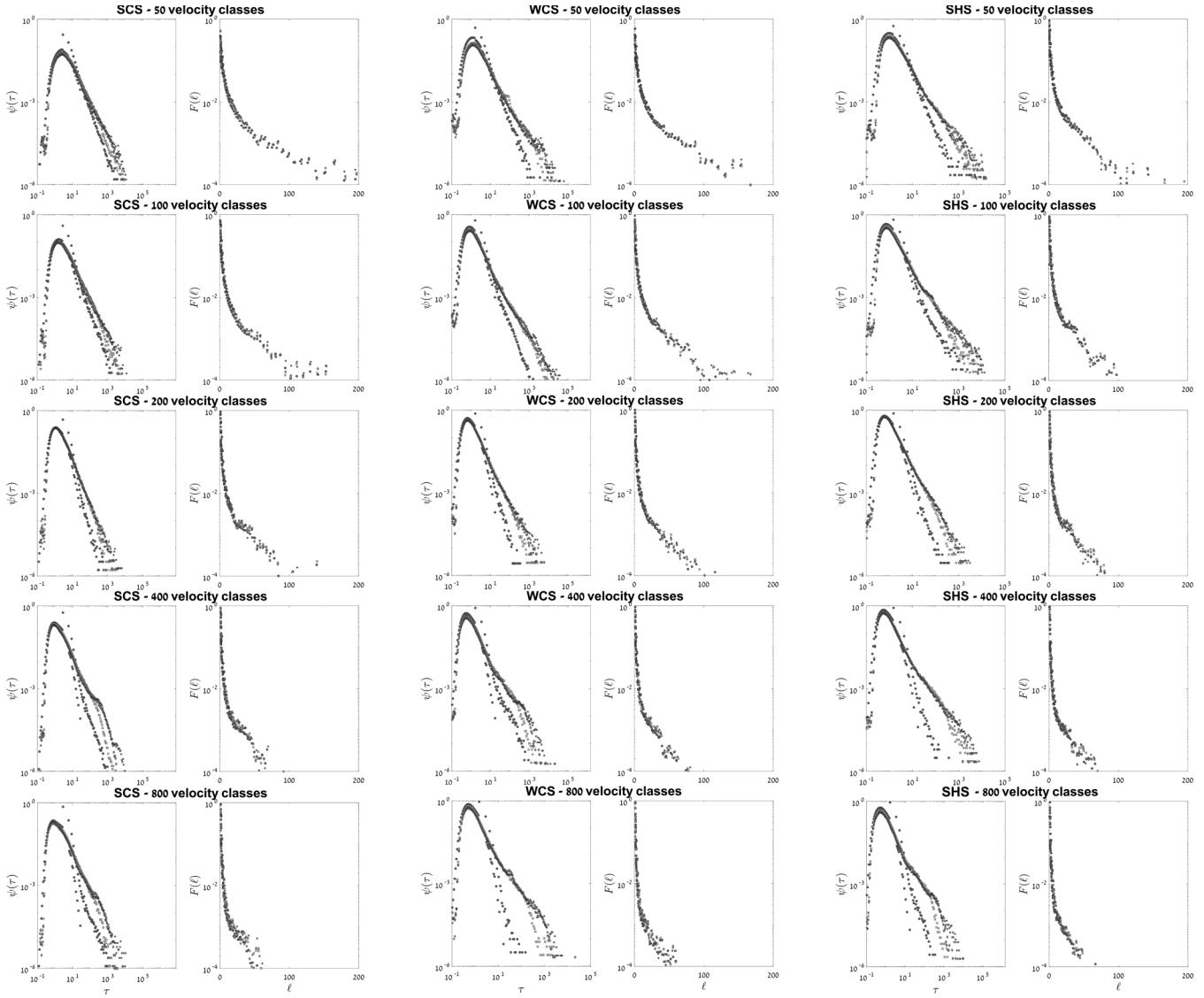

FIG. 9. Comparison between the effects of the number of velocity classes N on the shape of $\psi(t)$ and $F(\mathbf{s})$. Sensitivities are shown for $N = 50$ (first row), 100 (second row), and 200 (third row), 400 (fourth row), and 800 (fifth row), for the three types of porous systems (i.e., SCS, WCS, and SHS).

APPENDIX C: CTRW FRAMEWORK

In the CTRW-PT, the movement of each particle is governed by the equation of motion:

$$\mathbf{s}^{(N+1)} = \mathbf{s}^{(N)} + \boldsymbol{\varsigma}^{(N)}, \quad t^{(N+1)} = t^{(N)} + \tau^{(N)}, \tag{C1}$$

where a random spatial increment $\varsigma^{(N)}$ and a random temporal increment $\tau^{(N)}$ are assigned to each particle transition. For each N step, a velocity v can be derived by $\varsigma^{(N)}/\tau^{(N)}$. It is emphasized that a wide range of space-time couplings and/or correlations can be accounted for with this simulation methodology, by appropriate definition of the increments $\varsigma^{(N)}$ and $\tau^{(N)}$.

In the discussion here, a decoupled form of (C1) is employed; the space-time particle transition probability density function (PDF) $\psi(\mathbf{s}, t)$ can be written as

$$\psi(\mathbf{s}, t) = F(\mathbf{s})\psi(t), \tag{C2}$$

where $\varsigma^{(N)}$ and $\tau^{(N)}$ are chosen from distinct and independent PDFs for space and time, $F(\mathbf{s})$ and $\psi(t)$, respectively.

In this formulation, the mean particle velocity, v_ψ, and the generalized particle dispersion, D_ψ, are defined as the first and second spatial moments of $F(s)/\bar{t}$, respectively [3]. Here $\bar{t}$ denotes the mean time and $\bar{s}$ represents the mean step size (displacement length). We thus write for v_ψ and D_ψ in the direction of the flow:

$$v_\psi = \frac{\bar{s}}{\bar{t}} = \frac{\int_0^\infty F(s)s\,ds}{\int_0^\infty \psi(t)t\,dt} \tag{C3}$$

and

$$D_\psi = \frac{1}{2}\frac{\overline{s^2}}{\bar{t}} = \frac{1}{2}\frac{\int_0^\infty F(s)s^2\,ds}{\int_0^\infty \psi(t)t\,dt}. \tag{C4}$$

It is clear that the choice of PDFs $F(s)$ and $\psi(t)$ essentially determines the nature of the transport.

Following the direct numerical simulations, we use a curved power-law distribution for $\psi(t)$ and exponential distribution for $F(\mathbf{s})$;

$$\psi(t) = \frac{\exp\left[-\frac{(1+\beta)\tau^*}{t}\right]\left[\frac{(1+\beta)t^*}{t}\right]^\beta}{t\Gamma(\beta)} \tag{C5}$$

and

$$F(\mathbf{s}) = \lambda\exp(-\lambda\mathbf{s}); \tag{C6}$$

see Sec. III A for more information.

To obtain the relation between the mean particle velocity (C3) and the generalized longitudinal dispersion (C4) to the curved power-law parameters and the exponential distribution parameters, the integrals $\int_0^\infty \psi(t)t\,dt = \bar{t}$ and $\int_0^\infty F(s)s\,ds = \bar{s}$ must be defined. Inserting (C5) and (C6) into (C3) and (C4) yields

$$v_\psi = \frac{\beta-1}{(\beta+1)\lambda t^*} \tag{C7}$$

and

$$D_\psi = \frac{\beta-1}{(\beta+1)\lambda^2 t^*}. \tag{C8}$$

Thus $\bar{t} = \frac{(\beta+1)t^*}{(\beta-1)}$, $\bar{s} = \lambda^{-1}$, and $\overline{s^2} = 2\lambda^{-2}$.

[1] J. Bear, *Dynamics of Fluids in Porous Media* (American Elsevier, New York, 1972), p. 764.
[2] F. A. Dullien, in *Porous Media: Fluid Transport and Pore Structure* (Academic Press, San Diego, 1992), pp. 5–115.
[3] B. Berkowitz, A. Cortis, M. Dentz, and H. Scher, Rev. Geophys. **44**, 1 (2006).
[4] B. Bijeljic, A. Raeini, P. Mostaghimi, and M. J. Blunt, Phys. Rev. E **87**, 013011 (2013).
[5] Y. Edery, A. Guadagnini, H. Scher, and B. Berkowitz, Water Resour. Res. **50**, 1490 (2014).
[6] B. Berkowitz and H. Scher, Phys. Rev. Lett. **79**, 4038 (1997).
[7] B. Bijeljic, P. Mostaghimi, and M. J. Blunt, Phys. Rev. Lett. **107**, 204502 (2011).
[8] M. Dentz, P. K. Kang, A. Comolli, T. Le Borgne, and D. R. Lester, Phys. Rev. Fluids **1**, 074004 (2016).
[9] M. Dentz, M. Icardi, and J. J. Hidalgo, J. Fluid Mech. **841**, 851 (2018).
[10] V. Cvetkovic, H. Cheng, and X. H. Wen, Water Resour. Res. **32**, 1671 (2006).
[11] M. Bianchi, C. Zheng, C. Wilson, G. R. Tick, G. Liu, and S. M. Gorelick, Water Resour. Res. **47**, W05524 (2011).
[12] A. Nissan and B. Berkowitz, Phys. Rev. Lett **120**, 054504 (2018).
[13] J. J. Tessier, K. J. Packer, J.-F. Thovert, and P. M. Adler, AIChE J. **43**, 1653 (1997).
[14] J. J. Tessier and K. J. Packer, Phys. Fluids **10**, 75 (1998).
[15] U. M. Scheven, D. Verganelakis, R. Harris, M. L. Johns, and L. F. Gladden, Phys. Fluids **17**, 117107 (2005).
[16] W. Zhao, G. Picard, G. Leu, and P. M. Singer, Transp. Porous Media **81**, 305 (2010).
[17] P. K. Kang, M. Dentz, T. L. Borgne, S. Lee, and R. Juanes, Adv. Water Resour. **106**, 80 (2017).
[18] T. Le Borgne, D. Bolster, M. Dentz, P. de Anna, and A. Tartakovsky, Water Resour. Res. **47**, W12538 (2011).
[19] E. W. Montroll and H. Scher, J. Stat. Phys **9**, 101 (1973).
[20] M. Dentz, A. Cortis, H. Scher, and B. Berkowitz, Adv. Water Resour. **27**, 155 (2004).
[21] B. Berkowitz, S. Emmanuel, and H. Scher, Water Resour. Res. **44**, W03402 (2008).
[22] R. Seright and F. Martin, *Fluid Diversion and Sweep Improvement with Chemical Gels in Oil Recovery Processes, Second Annual Report*, report number DOE/BC/14447-15, DOE contract number FG22-89BC14447 (New Mexico Institute for Mining and Technology/New Mexico Petroleum Recovery Research Center, Albuquerque, 1992).
[23] S. E. Silliman, Water Resour. Res. **37**, 1883 (2001).
[24] B. Berkowitz and H. Scher, Adv. Water Resour. **32**, 750 (2009).
[25] J. P. Pereira Nunes, B. Bijeljic, and M. J. Blunt, Transp. Porous Media **109**, 317 (2015).
[26] T. Le Borgne, M. Dentz, and J. Carrera, Phys. Rev. Lett. **101**, 090601 (2008).
[27] H. Scher and M. Lax, Phys. Rev. B **7**, 4491 (1973).
[28] H. Scher and E. W. Montroll, Phys. Rev. B **12**, 2455 (1975).
[29] B. Berkowitz and H. Scher, Phys. Rev. E **81**, 011128 (2010).
[30] M. Dentz, H. Scher, D. Holder, and B. Berkowitz, Phys. Rev. E **78**, 041110 (2008).
[31] B. Bijeljic and M. J. Blunt, Water Resour. Res. **42**, W01202 (2006).
[32] G. Chabrier, Publ. Astron. Soc. Pac. **115**, 763 (2003).
[33] H. O. Pfannkuch, Rev. Inst. Fr. Petrole **18**, 215 (1963).
[34] B. Bijeljic, A. H. Muggeridge, and M. J. Blunt, Water Resour. Res. **40**, W11501 (2004).
[35] J. D. Seymour and P. T. Callaghan, AIChE J. **43**, 2096 (1997).
[36] M. E. Rhodes, B. Bijeljic, and M. J. Blunt, Adv. Water Resour. **31**, 1527 (2008).
[37] A. Nissan, I. Dror, and B. Berkowitz, Water Resour. Res. **53**, 3760 (2017).